Nano Research

Open Access

Research Article

Hierarchically porous N-doped carbon confined single-atom Fe catalyst for efficient electrochemical CO_2 reduction

Guanghuan Ma[1], Yang Chen[1] ✉, Hui Li[2,3], Ying Sun[1], Hua Fan[4], Shuoshuo Jiang[1], Xin Cui[1], and Tianyi Ma[2,3] ✉

[1] *Institute of Clean Energy Chemistry, Key Laboratory for Green Synthesis and Preparative Chemistry of Advanced Materials of Liaoning Province, College of Chemistry, Liaoning University, Shenyang 110036, China*
[2] *Centre for Atomaterials and Nanomanufacturing (CAN), School of Science, RMIT University, Melbourne, VIC 3000, Australia*
[3] *ARC Industrial Transformation Research Hub for Intelligent Energy Efficiency in Future Protected Cropping (E2Crop), Melbourne, VIC 3000, Australia*
[4] *Aqualux AU Pty Ltd, 12 Kanangra Cres, Clontarf, NSW 2093, Australia*

Cite this article: *Nano Research*, **2025**, *18*, 94907297. https://doi.org/10.26599/NR.2025.94907297

ABSTRACT: Electrochemical CO_2 reduction reaction (CO_2RR) is a promising process for reducing CO_2 emissions and producing high-value chemicals. However, this process remains hindered by diffusion-limited mass transfer, low activity, and high overpotentials. Here, we controllably prepared hierarchically porous nitrogen-doped carbon, carbon nanosheets, and carbon nanotubes confined single-atom Fe catalysts for electrochemical CO_2 reduction. The hierarchically porous Fe-N-C (Fe-HP) exhibited prominent performance with a Faradaic efficiency of CO (FE_{CO}) up to 80% and a CO partial current density (j_{CO}) of −5.2 mA·cm^{-2} at −0.5 V vs. reversible hydrogen electrode (RHE), far outperforming the single-atom Fe on N-C nanosheets (Fe-NS) and N-C nanotubes (Fe-NT). The detailed characterizations and kinetic analysis revealed that the hierarchically porous structure accelerated the mass transfer and electron transfer processes toward single-atom Fe sites, promoting the desorption of CO and thereby enhancing CO_2 reduction efficiency. This study provides a promising approach to designing efficient single-atom catalysts with porous structures for energy conversion applications.

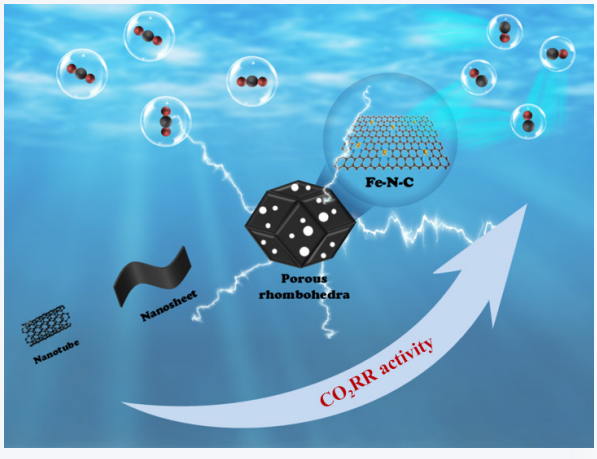

KEYWORDS: single-atom catalysts, Fe-N-C, CO_2 reduction, porous structure, electrocatalysis

1 Introduction

The massive burning of fossil fuels is accompanied by excessive CO_2 emissions [1–3]. This brings an unprecedented energy crisis and causes serious environmental pollution [4–6]. Electrochemical CO_2 conversion as a promising environmentally and friendly process has attracted significant attention in recent years [7–10]. However, the CO_2 molecule has high thermodynamic stability, and the bond energy of C=O (806 kJ·mol^{-1}) is too high to break it except under a high potential [11–13]. In addition, the slow reaction kinetics and the inevitable competitive hydrogen evolution reaction (HER) limit the energy conversion efficiency [14, 15]. Therefore, it is vital to develop effective catalysts with high selectivity and good stability.

Single-atom catalysts (SACs) with transition metal atoms anchored to nitrogen-doped carbon (N-C) have attracted much attention in recent years due to their high atomic utilization and unique structures [16–19]. The design of dual-structure SACs is found to promote activity through synergistic effects [20, 21]. Among them, Ni-N_x usually shows high selectivity for CO but suffers from weak binding to *COOH, resulting in higher overpotentials [22–24]. The Co-N-C is more likely to catalyze HER, because the energy barrier of CO desorption from Co-N_x sites is higher than that of competing H_2 [22, 25–27]. Compared with Ni and Co-based catalysts, Fe-N_x sites exhibit suitable binding to *COOH, resulting in lower overpotentials. However, Fe-N_x sites are strongly bound to CO, and they are inhibited by CO desorption,

Received: December 9, 2024; **Revised:** January 15, 2025
Accepted: February 10, 2025

✉Address correspondence to Yang Chen, yangchen@lnu.edu.cn; Tianyi Ma, tianyi.ma@rmit.edu.au

thus resulting in poor activity [23, 25, 28, 29]. Therefore, it is necessary to further improve the catalytic performance of Fe-based catalysts.

Significant studies have been devoted to improving the catalytic performance of Fe-N-C. For instance, Wu et al. successfully constructed an axially coordinated Fe-N_5 structure for CO_2 reduction reaction (CO_2RR) [30]. The optimized catalyst reduced the energy barrier of CO desorption and inhibited the generation of H_2. Chen et al. introduced phosphorus to adjust the chemical state of Fe to form Fe-N_3P sites, which decreased the free energy barrier for the adsorption and activation of CO_2 [31]. In addition, constructing asymmetrical coordination structures via sulfur, nitrogen-codoping or incorporating Sn atom to anchor Fe dual atoms was found to improve catalytic performance [32–34]. Moreover, Li et al. eliminated the uncoordinated N in Fe-N-C through a hydrogen-pyrolysis strategy, thus promoting the activation and protonation of CO_2 [35]. In addition to intrinsic activity, modulating the structure and morphology of supports to expose more active sites and improve the mass transfer is also significant in boosting catalytic performance. Zhao et al. optimized the carbon carrier with the assistance of polystyrene microspheres, which reduced mass transfer resistance while accelerating the diffusion of the gas [36]. Based on the Kirkendall effect, Chen et al. effectively increased the specific surface area of the N-C carrier with the help of oxalate, thus improving the selectivity of Fe-N-C to CO [37]. However, previous studies involving N-C supports anchoring single atoms mainly show three-dimensional bulk features, resulting in some active sites buried and insufficient mass transfer process. The shape effect of N-doped carbon substrates on single-atom metal centers and catalytic performance needs to be further elucidated.

Herein, we successfully anchored Fe single atoms to three different morphologies of carbon carriers through controllable synthesis, including hierarchically porous carbon (Fe-HP), carbon nanosheets (Fe-NS), and carbon nanotubes (Fe-NT). The Fe-HP consisting of micropores, mesopores, and macropores exhibited high activity and selectivity for CO_2 reduction to CO with a maximum of 80% of FE_{CO} at −0.5 V vs. reversible hydrogen electrode (RHE), which was about 2.5 times than that of Fe-NS and nearly 12 times than that of Fe-NT. In addition, the Fe-HP achieved a high partial current density of CO of −9.1 mA·cm^{-2} and a high turnover frequency (TOF) value of 1372 h^{-1} at −0.8 V vs. RHE even with a low metal loading (0.35 wt.%), which was comparable to the current state-of-the-art Fe SACs. Detailed characterization and kinetic analysis showed that the hierarchically porous structure facilitated the exposure of active sites and reduced the valence state of Fe centers. The relatively low valence state of Fe and its porous structure benefited CO_2 activation and promoted the desorption of CO, thereby boosting CO_2 reduction performance.

2 Experimental sections

2.1 Catalysts preparation

2.1.1 *Synthesis of Fe-HP*

The Fe-HP was synthesized by the pyrolysis strategy of doped surfactant P123 [38, 39]. First, 4.165 g of 2-methylimidazole was dissolved in 100 mL of methanol, 8.045 g of $Zn(NO_3)_2{\cdot}6H_2O$ was dissolved in 120 mL of methanol, 2.0 g of surfactant P123 was dissolved in 20 mL of methanol. The three solutions were mixed and stirred at room temperature for 24 h. Then, the obtained suspension was separated by centrifuging and washed with methanol. After drying at 60 °C, the P123/ZIF-8 was obtained. Second, 100 mg of P123/ZIF-8 was dispersed in 15 mL of methanol. Afterward, 50 μL of 100 mg·mL^{-1} $Fe(NO_3)_3{\cdot}9H_2O$ aqueous solution was added to the methanol solution to obtain the Fe/P123/ZIF-8. Finally, to obtain the Fe-HP, the Fe/P123/ZIF-8 was treated at 1000 °C under an Ar-atmosphere for 2 h.

2.1.2 *Synthesis of Fe-NS*

The Fe-NS was synthesized by molten salt assisted pyrolysis [40]. First, 3.4 g of 2-methylimidazole was dissolved in 150 mL of methanol in a round-bottom flask, followed by the addition of 150 mL of methanol solution containing 2.97 g of $Zn(NO_3)_2{\cdot}6H_2O$ and 8 mg of $Fe(NO_3)_3{\cdot}9H_2O$. The mixture was stirred at 60 °C for 24 h. Afterward, the obtained suspension was separated by centrifuging and washed with methanol. After drying at vacuum oven at 60 °C, the Fe/ZIF-8 was obtained. Second, 300 mg of Fe/ZIF-8, 1.08 g of KCl, and 1.92 g of $ZnCl_2$ were mixed together and ground. Then the solid was treated at 900 °C for 2 h under a flowing N_2-atmosphere. After cooling down, the black solid was washed with deionized water. Finally, after drying at vacuum oven at 60 °C, the Fe-NS was obtained.

2.1.3 *Synthesis of Fe-NT*

The Fe-NT sample was prepared by a simple impregnation strategy. First, 50 mg of nitrogen-doped carbon nanotubes (NCNTs) was dispersed in 15 mL of methanol with the aid of ultrasound. Then 140 μL 25 mg·mL^{-1} of an aqueous solution of $Fe(NO_3)_3{\cdot}9H_2O$ was added and stirred for 5 h. After the adsorption process, the solvent was dried at 80 °C and fully ground. To obtain the final sample, the dried carbon nanotubes were calcined in the Ar-atmosphere at 600 °C for 1 h.

2.2 Catalyst characterization

Scanning electron microscopy (SEM) images were obtained on a JSM-7800F instrument to observe the shapes of all the samples. High-resolution transmission electron microscopy (HRTEM) images, aberration-corrected high-angle annular dark-field scanning transmission electron-microscopy (AC-HAADF-STEM), and energy-dispersive X-ray spectroscopy (EDS) mapping images were obtained on a JEOL JEM-ARM200F instrument.

The Brunauer–Emmett–Teller (BET) surface area was measured on a Micromeritics ASAP 2460 at 77 K by N_2 adsorption and desorption. Based on the Barrett–Joyner–Halenda (BJH) theory, the pore size distribution of three samples was obtained. The results of X-ray powder diffraction (XRD) were collected over on an X' Pert Pro X-ray diffractometer with Cu Kα (λ = 0.15432 nm) radiation at 40 kV and 30 mA, the test angles (2θ) ranged from 10° to 80°. The Raman spectra were recorded on a NanoWizard Raman spectrometer using a 633 nm laser as the excitation source.

The contents of metal species were measured by inductively coupled plasma optical emission spectroscopy (ICP-OES) on an ICPS-7300DV instrument (Perkin Elmer). The valence state and coordination structure of the metal active center of the catalyst were determined by X-ray photoelectron spectroscopy (XPS) on a Thermo Fisher ESCALAB 250XI with a monochromatic Al Kα X-ray source. All electron binding energy of all elements was calibrated by using the C 1s energy of amorphous carbon (284.80 eV).

The CO_2 and CO temperature programmed desorption (CO_2-TPD and CO-TPD) were performed on an Auto Chem II 2920 automatic catalyst characterization system with online mass spectroscopy (MS) analysis.

2.3 Electrochemical measurement

Electrochemical measurements were collected on an electrochemical workstation (CHI 760E) using an H-type cell separated by a proton exchange membrane (Nafion-117). Each compartment was filled with 70 mL 0.5 M $KHCO_3$ aqueous solution as electrolyte. The three-electrode system was composed of carbon paper supported by catalyst as the working electrode, Ag/AgCl as the reference electrode, and Pt plate as the opposite electrode. The working electrode of the supported catalyst was prepared according to the following steps. Firstly, 4 mg of catalyst powder, 200 μL of deionized water, 170 μL of ethanol, and 30 μL of Nafion solution (5 wt.%) were mixed together and sonicated for 30 min to obtain the uniform catalyst ink. Secondly, the ink was dropped onto a carbon paper (1 cm × 2 cm), the loading amount of the catalyst was about ~ 1 mg·cm^{-2}. Linear sweep voltammogram (LSV) tests of three samples were carried out with a scan rate of 10 mV·s^{-1} in Ar-saturated and CO_2-saturated 0.5 M $KHCO_3$. In order to ensure Ar-saturated or CO_2-saturated atmosphere, the corresponding gas was pumped in for at least 30 min before the test and the flow of gas was maintained during the electrolysis with the flow rate of 30 mL·min^{-1}.

The catalytic performance of the catalyst was tested by the controlled potential electrolysis method, and the test voltage range was from −0.3 to −0.9 V vs. RHE. During the test, the applied potential was successively increased, and the constant potential electrolysis was maintained at each potential for at least 1 h. The gas phase products produced at each potential were determined by a gas chromatograph (GC, BFRL SP-3400). The gas chromatograph was equipped with a thermal conductivity detector (TCD) for quantifying H_2 and a flame ionization detector (FID) for quantifying CO. To determine the potential liquid phase products in the electrolysis process, the reaction electrolyte was analyzed by nuclear magnetic resonance (^{1}H NMR). To evaluate the activity, selectivity, and energy utilization efficiency of the catalyst, the Faradaic efficiency of each product was calculated separately, and the calculation method was referred to the following Eq. (1)

$$FE_{CO} = 2 \times F \times (A/Q) \times [273/(273+T)] \times 100 \quad (1)$$

where FE (%) is the Faradaic efficiency of each product during electrolysis, F is Faraday's constant (96,485 C·mol^{-1}), A (mol) is the number of moles of each gas phase product, which can be obtained by the equation: $A = X \times 10^{-6}/22.4$, where X is directly measured by GC, Q (C) is the total amount of electricity during the electrolysis process, T (°C) is the temperature at which the electrolysis process took place. During the entire testing process, all of the potentials measured by the Ag/AgCl electrode were converted to the RHE according to the following Eq. (2)

$$E\,(\text{V vs. RHE}) = E\,(\text{V vs. Ag/AgCl}) + 0.197\ \text{V} + 0.059 \times \text{pH} \quad (2)$$

In addition, in order to further explore the mechanism of the catalyst in terms of reaction kinetics, we also tested data such as electrochemical surface area (ECSA), Tafel slope, and electrochemical impedance spectroscopy (EIS). ECSA was obtained by double-layer capacitance (C_{dl}) fitting through cyclic voltammetry (CV) curves at different scanning speeds (1 to 6 mV·s^{-1}). EIS was measured at an open-circuit voltage (OCP) with a frequency of 1 to 500,000 Hz and an amplitude of 5 mV.

3 Results and discussion

3.1 Synthesis and structural characterization

The Fe-N-C SACs with different morphologies were synthesized by controllable high-temperature pyrolysis, which could be universal to synthesize other metal-N-C SACs. As presented in Fig. 1(a), the Fe-HP was prepared by adding the surfactant P123 during the synthesis of the precursors. In the process of pyrolysis, the P123 copolymer effectively induced the formation of hierarchically porous structure. The Fe-NS was synthesized by a molten salt-assisted pyrolysis strategy. At high temperature, Fe/ZIF-8 was carbonized, while the generated carbon fragments combined and rearranged to form two-dimensional micron-scale nanosheets under the induction of salt ions [41–43]. The Fe-NT was prepared by impregnation-pyrolysis approach due to the NCNTs with rich nitrogen content and good adsorption capacity.

The structural and morphology features of catalysts were characterized by SEM and TEM. The SEM (Fig. 1(b)) and TEM images (Fig. 1(c)) of Fe-HP showed that the catalyst maintained a typical rhombohedral shape of ZIF-8. The average particle size of the Fe-HP was about 104 nm (Fig. S1(a) in the Electronic Supplementary Material (ESM)), which might be beneficial for improving the rate of diffusion of reactants and products [44]. As shown in Fig. S1(b) in the ESM, there was no metal cluster or nanoparticle on the amorphous carbon support, suggesting the high dispersion of metal species. The AC-HAADF-STEM images of Fe-HP (Fig. 1(d) and Fig. S1(d) in the ESM) illustrated that there were bright spots dispersed on the N-C substrate. Combined with the electron energy loss spectroscopy (EELS), it confirmed the formation of Fe single atoms (Figs. S1(d) and S1(e) in the ESM). The corresponding EDS showed that the C, N, and Fe elements were uniformly distributed on the entire polyhedron (Fig. 1(e)). The above characterization results strongly proved the success of the synthesis of atomically dispersed catalysts. As shown in Fig. S2(a) in the ESM, Fe-NS presented a two-dimensional micron-scale thin nanosheet structure and the image of HRTEM (Fig. S2(b) in the ESM) showed that it also presented an amorphous structure. Moreover, the Fe-NT still maintained the hollow tubular structure after impregnation and pyrolysis (Figs. S3(a) and S3(b) in the ESM). Similar to the Fe-HP, Fe single atoms were also observed on the NS and NT carriers in the AC-HAADF-STEM images of Fe-NS (Fig. S2(c) in the ESM) and Fe-NT (Fig. S3(c) in the ESM). The EDS mappings of the Fe-NS (Fig. S2(d) in the ESM) and the Fe-NT (Fig. S3(d) in the ESM) confirmed the uniform distribution of C, N, and Fe on the carbon carriers. The contents of Fe determined by ICP-OES of Fe-HP, Fe-NS, and Fe-NT were 0.35 wt.%, 1.16 wt.%, and 0.53 wt.%, respectively. The consistent loading of Fe in the catalysts allowed us to directly compare the CO_2 reduction activities of different Fe-N-C catalysts and explore the effect of carbon carrier morphology.

XRD of Fe-HP, Fe-NS, and Fe-NT showed only the diffraction peaks of carbon species (Fig. 2(a)), and there was no diffraction peak of any metal, suggesting high dispersion of Fe species, which was consistent with HRTEM results. In addition, Fe-HP and Fe-NS

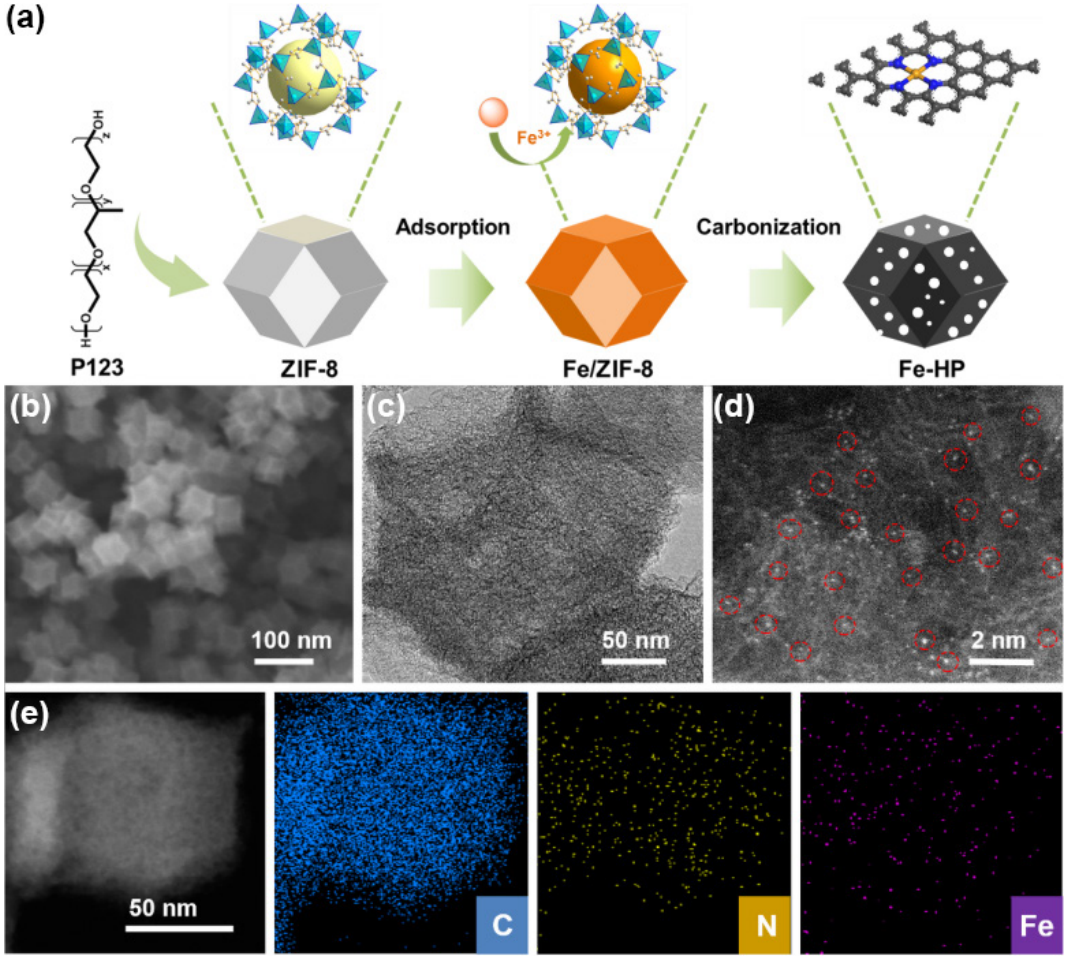

Figure 1 (a) The synthesis route of Fe-HP. (b) SEM image of Fe-HP. (c) TEM image of Fe-HP. (d) AC-HAADF-STEM image of Fe-HP and (e) EDS mappings of Fe-HP.

showed two diffraction peaks at 24° and 44°, corresponding to the (002) and (101) planes of graphitized carbon, respectively [45]. Raman spectra of Fe-HP, Fe-NS, and Fe-NT displayed two peaks (Fig. 2(b)) at about 1350 and 1590 cm^{-1}, corresponding to the typical D band and G band [46, 47]. The strength ratio between the D band and G band (I_D/I_G) was calculated, the I_D/I_G ratios were 0.97, 0.96, and 0.43 in Fe-HP, Fe-NS, and Fe-NT. It was found that the I_D/I_G ratio of Fe-NT (0.43) was lower than that of Fe-HP (0.97) and Fe-NS (0.96), indicating that Fe-NT had a higher graphitization degree [44]. Besides, it was found that the ratio gradually decreased, indicating that the Fe-HP exhibited the highest degree of structural defect density, which might originate from the developed porosity [40, 47–49]. The BET surface area of three samples was determined by N_2 adsorption and desorption isotherms. As shown in Fig. 2(c) and Table S1 in the ESM, the BET surface area of Fe-HP was up to 1555.83 $m^2 \cdot g^{-1}$, which was higher than Fe-NS of 1399.62 $m^2 \cdot g^{-1}$ and Fe-NT of 109.48 $m^2 \cdot g^{-1}$. The physical adsorption isotherm of the Fe-HP could be classified as type IV, and the hysteresis loop as class H4, which indicated that there were a considerable number of micropores and mesopores on the surface of Fe-HP and speculated that the Fe-HP was hierarchically porous [50]. The pore size distributions were further analyzed (Fig. 2(d) and Table S1 in the ESM). Obviously, the Fe-HP showed distinctive pore size distribution characteristics with a sharp peak at < 2 nm, indicating the presence of micropores on the surface of the Fe-HP. In addition, there were two peaks at 4 nm and > 30 nm, indicating that there were also mesopores and macropores on the surface of the Fe-HP, which further confirmed the successful formation of the hierarchically porous structure. The Fe-NS only showed a sharp peak at 2–3 nm, indicating that mesopores contributed almost all of the pore volume. And there were no micropores or macropores on the surface of the Fe-NS. The surface of the Fe-NT was almost entirely composed of macropores. These results indicated that the as-prepared catalysts had completely different pore size distribution characteristics.

The valence state of the Fe centers was further analyzed by XPS. As shown in Fig. 3(a), Fe-HP, Fe-NS, and Fe-NT contained only four elements as C, N, O, and Fe. According to the Fe 2p spectra (Fig. 3(b)), the binding energy of Fe $2p_{3/2}$ in Fe-HP (710.4 eV), Fe-NS (711.3 eV), and Fe-NT (711.8 eV) located between Fe^{2+} and Fe^{3+}, suggesting the partially oxidative state of Fe [51]. Meanwhile, Fe $2p_{3/2}$ in Fe-HP shifted to a lower energy than that in Fe-NS and in Fe-NT. The Fe 2p XPS results indicated that the Fe atoms obtained more electrons, resulting in a relatively low oxidative state of the Fe centers [51, 52]. As shown in Fig. 3(c), the N 1s spectra of all catalysts were convolved into five peaks for N species, corresponding to pyridinic N (398.5 eV), Fe–N_x (399.2 eV), pyrrolic N (400.3 eV), graphitic N (401.0 eV), and oxidized N (402.7 eV) [38, 53]. The peak at 399.2 eV can be attributed to the metal–N coordination, indicating the existence of the Fe–N

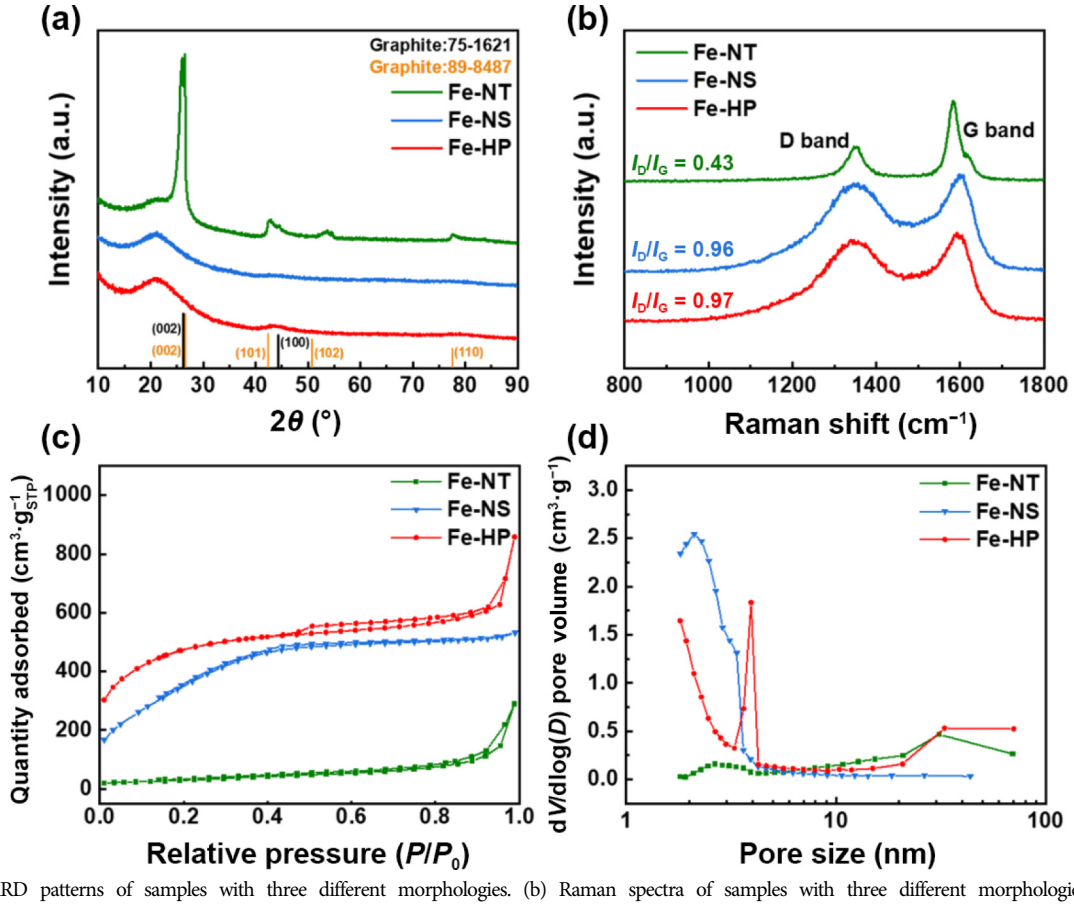

Figure 2 (a) XRD patterns of samples with three different morphologies. (b) Raman spectra of samples with three different morphologies. (c) Nitrogen adsorption–desorption curves and BET surface area of samples with three different morphologies. (d) Pore size distribution curves of samples with three different morphologies.

coordination. In addition, calculating the proportion of each N species, it was found that Fe-HP had more Fe-N coordination structures (Fig. 3(d)), which might be due to its well-developed pore structures. The above results showed that the coordination structures of Fe were similar among the as-prepared catalysts, but the electronic properties of Fe centers were different.

3.2 Electrochemical CO_2RR performance

The electrochemical CO_2RR performance of as-prepared catalysts was measured in a CO_2-saturated 0.5 M $KHCO_3$ solution by using an H-type cell. LSV was measured from 0 to −1.2 V vs. RHE with a scan rate of 10 mV·s^{-1} in Ar-saturated and CO_2-saturated, respectively. Obviously, the current densities of all catalysts in the CO_2-saturated electrolytes were higher than that in the Ar-saturated electrolytes (Fig. S4 in the ESM), indicating the occurrence of the electrochemical reduction of CO_2. In the CO_2-saturated electrolyte, the Fe-HP showed the highest current density, followed by the Fe-NS and the smallest Fe-NT (Fig. 4(a)). Furthermore, constant potential electrolysis was performed in the range of −0.3 to −0.9 V vs. RHE for 1 h. The types and contents of gaseous products were detected by GC and potential liquid products were detected by ^{1}H NMR. As shown in Fig. 4(b), Fe-HP achieved the maximum FE_{CO} of 80% at −0.5 V vs. RHE, which was significantly higher than that of Fe-NS (~ 38%) and Fe-NT (~ 7%), comparable to most of the previously reported Fe-based catalysts (Table S2 in the ESM). It was worth noting that the three morphologies of carbon carriers (HP, NS, and NT) showed inferior activity and selectivity (Fig. S5 in the ESM), suggesting that the Fe species were active centers for CO_2RR. As shown in Fig. 4(c), the CO partial current density of the Fe-HP reached 9.1 mA·cm^{-2} at −0.8 V vs. RHE, which was about two times higher than that of the Fe-NS and five times to Fe-NT. The ^{1}H-NMR and GC analyses suggested the main products were gaseous products, and no liquid products were detected (Fig. S7 in the ESM). To compare the intrinsic activity, the turnover frequency (TOF) values were calculated (Fig. 4(d)). It was found that the Fe-HP exhibited the highest TOF value of 1372 h^{-1} at −0.8 V vs. RHE, which was much higher than that of Fe-NS (264 h^{-1}) and Fe-NT (175 h^{-1}). And the TOF value of the Fe-HP at −0.8 V vs. RHE was higher than most of the current state-of-the-art SACs (Fig. 4(e)) [31, 44, 54–59]. In order to determine the durability, a continuous electrolytic test was carried out. The FE_{CO} of the Fe-HP was maintained at about 80% for 12 h (Fig. 4(f)), indicating the excellent stability of the Fe-HP. The characterization of catalyst after electrolysis showed that the Fe-HP still maintained a good polyhedral morphology and the Fe was still dispersed atomically (Fig. S8 in the ESM), which indicated that the Fe-HP exhibited remarkable durability.

3.3 Reaction kinetics study

To investigate the intrinsic reason for the excellent catalytic activity, we carried out a series of kinetic studies. The electrochemical surface area was obtained by the double-layer capacitance (C_{dl}) test in cyclic voltammetry at different scan rates. As shown in Fig. 5(a) and Fig. S6 in the ESM, the C_{dl} of Fe-HP was 40.2 mF·cm^{-2}, which

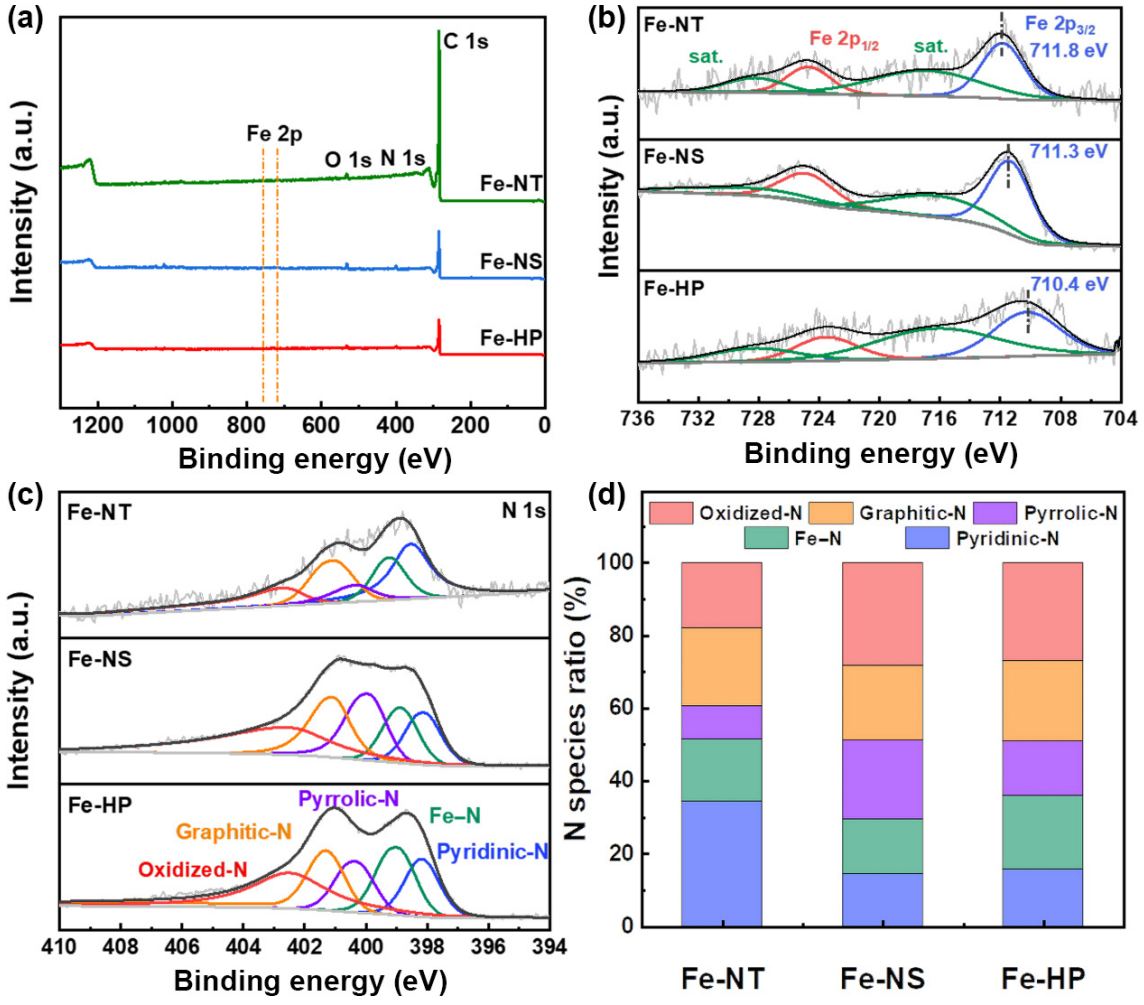

Figure 3 (a) XPS survey spectra of samples with three different morphologies. (b) Fe 2p XPS spectra. (c) N 1s XPS spectra and (d) the proportion of different kinds of N species.

was much higher than that of Fe-NS (36.4 mF·cm^{-2}) and Fe-NT (4.5 mF·cm^{-2}), indicating that the hierarchically porous structure could provide more active sites for CO_2RR. The Tafel slope is an important parameter to evaluate the reaction kinetics, and a smaller Tafel slope indicates a faster electron transfer rate, leading to a faster reaction rate. As shown in Fig. 5(b), it was found that the Fe-HP exhibited a small Tafel slope of 109.5 mV·dec^{-1}, lower than Fe-NS of 134.5 mV·dec^{-1} and Fe-NT of 232.6 mV·dec^{-1}, which indicated the rapid electron transfer and catalytic process on the porous surface [51, 60]. Moreover, electrochemical impedance spectroscopy was carried out to gain further insight into the kinetics. The high-frequency ohmic resistance (R_s) mainly originated from all contact resistances and the electrolyte. And the charge transfer resistance (R_{ct}) is related to the electrocatalytic kinetics [51, 61]. Thus, the lower R_{ct} suggests a faster reaction rate. As shown in Fig. S9 in the ESM, the R_{ct} values of the HP, NS, and NT are 3.4, 4.6, and 5.6 Ω, respectively. The incorporation of Fe decreased the R_{ct} values. The R_{ct} of Fe-HP (2.7 Ω) was lower than those of Fe-NS (2.9 Ω) and Fe-NT (4.1 Ω) (Fig. 5(c)), indicating the faster electron transfer kinetics of Fe-HP. These results verified that a hierarchically porous structure promoted the kinetics of electron transfer during the CO_2 to CO.

Besides, the adsorption properties of reaction molecules were investigated. According to the result of CO_2-TPD (Fig. S10 in the ESM), the CO_2 desorption peak of the Fe-HP was located at the temperature of 243 °C, which was higher than that of Fe-NS (237 °C) and Fe-NT (221 °C). This result indicated the strongest binding strength of CO_2 on Fe-HP, which facilitated the activation of CO_2 and the formation of *COOH [61]. Considering the desorption of CO was the rate-determining step (RDS) of CO_2 reduction on Fe SACs, the adsorption strength of CO was further investigated [22, 62, 63]. As shown in Fig. 5(d), the CO desorption peak of the Fe-HP was located at a relatively low temperature of −15 °C, which indicated that the hierarchically porous structure effectively promoted CO desorption. Comparatively, the desorption peaks of CO on Fe-NS and Fe-NT were located at higher temperatures (219 and 325 °C, respectively), which indicated that CO was difficult to desorp from the active sites, thus reducing the performance of CO_2RR. The facile desorption of CO on the Fe-HP surface could be due to the relatively low oxidation state of Fe centers. On the hierarchically porous substrate, the partially oxidative state of Fe facilitates the desorption of CO, thus speeding up the reaction kinetics [52]. Based on the above results and previous studies, it was proved that the hierarchically porous structure facilitated electron transfer and promoted the desorption of CO on Fe-N_4 sites (Fig. 5(e)), thus enhancing the catalytic performance [36, 38, 44].

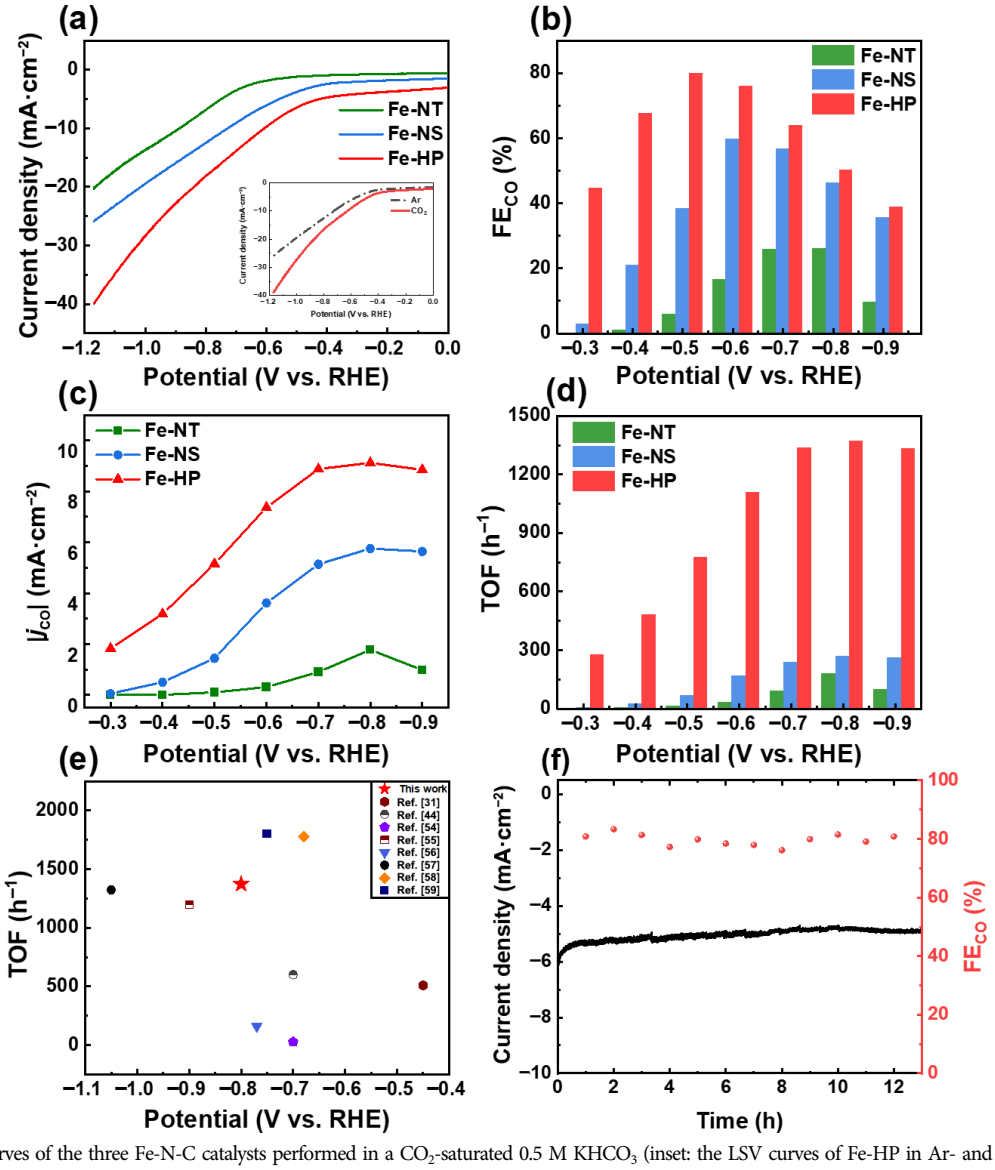

Figure 4 (a) LSV curves of the three Fe-N-C catalysts performed in a CO_2-saturated 0.5 M $KHCO_3$ (inset: the LSV curves of Fe-HP in Ar- and CO_2-saturated 0.5 M $KHCO_3$). (b) FE of CO on the three Fe-N-C catalysts at different potentials. (c) Partial current densities of CO. (d) TOF values of the three Fe-N-C catalysts. (e) Comparison of values of TOF and (f) stability test of the Fe-HP at −0.5 V vs. RHE.

4 Conclusions

In summary, simple and facile strategies were put forward to construct single-atom Fe-N-C catalysts with different morphologies for electrochemical CO_2 reduction. The obtained Fe-HP achieved a high FE_{CO} of up to 80% and partial CO current density of −5.2 mA·cm^{-2} at −0.5 V vs. RHE, which were higher than those of the Fe-NS and Fe-NT. A series of characterization and kinetic analyses showed that unique hierarchically porous structure increased the exposure of the active sites and accelerated the mass transfer process. Furthermore, the partially oxidative state of Fe centers on the porous carbon carrier facilitated the electron transfer process and promoted the desorption of CO, which greatly improved the CO_2 reduction performance of Fe-HP. This work highlights the crucial role of carbon carrier morphology and provides a new approach to enhanced catalysis by creating porous structures.

Electronic Supplementary Material: Supplementary material (further details of experimental sections and more characterization results) is available in the online version of this article at https://doi.org/10.26599/NR.2025.94907297.

Data availability

All data needed to support the conclusions in the paper are presented in the manuscript and the Electronic Supplementary Material. Additional data related to this paper may be requested from the corresponding author upon request.

Acknowledgements

This work was supported by the Australian Research Council (ARC) through Future Fellowship (FT210100298), Discovery Project (DP220100603), Linkage Project (LP210200504, LP220100088, LP230200897) and Industrial Transformation Research Hub (IH240100009) schemes, the China Postdoctoral Science Foundation (2023M743430), the Australian Government

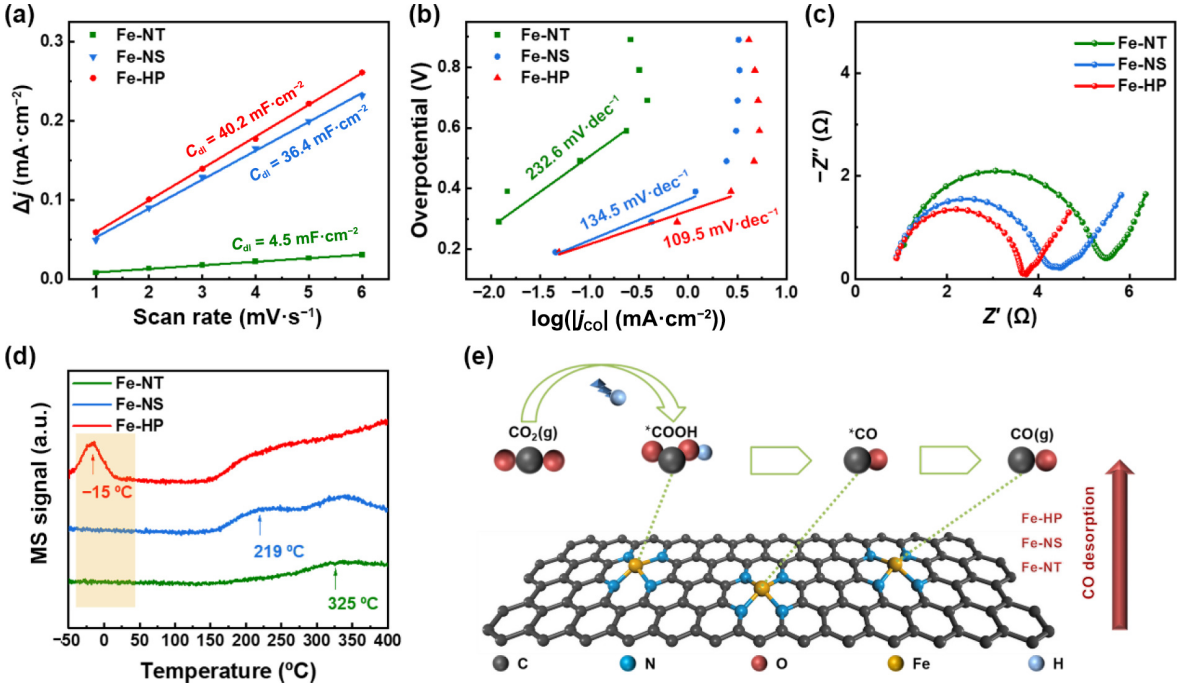

Figure 5 (a) Current density differences plotted against scan rates. (b) Tafel slopes of the three Fe-N-C catalysts. (c) Nyquist plots. (d) CO-TPD profiles for three catalysts. (e) Illustration of the possible pathway for electrocatalytic CO_2 reduction on the Fe-HP catalyst.

through the Cooperative Research Centres Projects (CRCPXIII000077), the Australian Renewable Energy Agency (ARENA) as part of ARENA's Transformative Research Accelerating Commercialisation Program (TM021), and European Commission's Australia-Spain Network for Innovation and Research Excellence (AuSpire).

Declaration of conflict of interest

The authors declare no conflict of interest.

Author contribution statement

G. H. M. carried out the experiments, analyzed data, and wrote the draft. Y. C. conceptualized and designed the experiments, performed structural characterizations, reviewed and revised the manuscript. H. L. analyzed data. Y. S. analyzed data. S. S. J. and X. C. collected and analyzed experimental data. H. F. analyzed data. T. Y. M. provided resources, reviewed, and revised the manuscript.

Use of AI statement

None.

References

[1] Turner, J. A. A realizable renewable energy future. *Science* **1999**, *285*, 687–689.

[2] Chu, S.; Cui, Y.; Liu, N. The path towards sustainable energy. *Nat. Mater.* **2017**, *16*, 16–22.

[3] Piao, S. L.; Ciais, P.; Huang, Y.; Shen, Z. H.; Peng, S. S.; Li, J. S.; Zhou, L. P.; Liu, H. Y.; Ma, Y. C.; Ding, Y. H. et al. The impacts of climate change on water resources and agriculture in China. *Nature* **2010**, *467*, 43–51.

[4] Falkowski, P.; Scholes, R. J.; Boyle, E.; Canadell, J.; Canfield, D.; Elser, J.; Gruber, N.; Hibbard, K.; Högberg, P.; Linder, S. et al. The global carbon cycle: A test of our knowledge of earth as a system. *Science* **2000**, *290*, 291–296.

[5] Zhang, J.; Guo, C. X.; Fang, S. S.; Zhao, X. T.; Li, L.; Jiang, H. Y.; Liu, Z. Y.; Fan, Z. Q.; Xu, W. G.; Xiao, J. P. et al. Accelerating electrochemical CO_2 reduction to multi-carbon products via asymmetric intermediate binding at confined nanointerfaces. *Nat. Commun.* **2023**, *14*, 1298.

[6] Li, L.; Li, X. D.; Sun, Y. F.; Xie, Y. Rational design of electrocatalytic carbon dioxide reduction for a zero-carbon network. *Chem. Soc. Rev.* **2022**, *51*, 1234–1252.

[7] Fang, W. S.; Lu, R. H.; Li, F. M.; He, C. H.; Wu, D.; Yue, K. H.; Mao, Y.; Guo, W.; You, B.; Song, F. et al. Low-coordination nanocrystalline copper-based catalysts through theory-guided electrochemical restructuring for selective CO_2 reduction to ethylene. *Angew. Chem., Int. Ed.* **2024**, *63*, e202319936.

[8] Ye, L.; Ying, Y. R.; Sun, D. R.; Zhang, Z. Y.; Fei, L. F.; Wen, Z. H.; Qiao, J. L.; Huang, H. T. Highly efficient porous carbon electrocatalyst with controllable N-species content for selective CO_2 reduction. *Angew. Chem., Int. Ed.* **2020**, *59*, 3244–3251.

[9] Akter, T.; Barile, C. J. Membrane-controlled CO_2 electrocatalysts with switchable C_2 product selectivity and high faradaic efficiency for ethanol. *J. Mater. Chem. A* **2023**, *11*, 11354–11363.

[10] Wei, B.; Xiong, Y. S.; Zhang, Z. Y.; Hao, J. H.; Li, L. H.; Shi, W. D. Efficient electrocatalytic reduction of CO_2 to HCOOH by bimetallic In-Cu nanoparticles with controlled growth facet. *Appl. Catal. B* **2021**, *283*, 119646.

[11] Pan, Q.; Chen, Y.; Jiang, S. S.; Cui, X.; Ma, G. H.; Ma, T. Y. Insight into the active sites of M-N-C single-atom catalysts for electrochemical CO_2 reduction. *EnergyChem* **2023**, *5*, 100114.

[12] Jin, S.; Hao, Z. M.; Zhang, K.; Yan, Z. H.; Chen, J. Advances and challenges for the electrochemical reduction of CO_2 to CO: From fundamentals to industrialization. *Angew. Chem., Int. Ed.* **2021**, *60*, 20627–20648.

[13] Zhang, Q. C.; Liu, D.; Zhang, Y. P.; Guo, Z. L.; Chen, M. P.; Chen, Y. Y.; Jin, B.; Song, Y. Z.; Pan, H. Insight into coupled Ni-Co dual-metal atom catalysts for efficient synergistic electrochemical CO_2 reduction. *J. Energy Chem.* **2023**, *87*, 509–517.

[14] Ping, D.; Huang, S. G.; Wu, S. D.; Zhang, Y. F.; Yi, F.; Han, L. F.; Wang, S. W.; Wang, H.; Yang, X. Z.; Guo, D. J. et al. LDHs-based bifunctional electrocatalyst for effective tunable syngas generation via CO_2 reduction. *Int. J. Hydrogen Energy* **2022**, *47*, 23653–23660.
[15] Abdinejad, M.; Dao, C.; Zhang, X. A.; Kraatz, H. B. Enhanced electrocatalytic activity of iron amino porphyrins using a flow cell for reduction of CO_2 to CO. *J. Energy Chem.* **2021**, *58*, 162–169.
[16] Cui, T. T.; Li, L. X.; Ye, C. L.; Li, X. Y.; Liu, C. X.; Zhu, S. H.; Chen, W.; Wang, D. S. Heterogeneous single atom environmental catalysis: Fundamentals, applications, and opportunities. *Adv. Funct. Mater.* **2022**, *32*, 2108381.
[17] Wang, A. Q.; Li, J.; Zhang, T. Heterogeneous single-atom catalysis. *Nat. Rev. Chem.* **2018**, *2*, 65–81.
[18] Chen, Y.; Lin, J.; Jia, B. H.; Wang, X. D.; Jiang, S. Y.; Ma, T. Y. Isolating single and few atoms for enhanced catalysis. *Adv. Mater.* **2022**, *34*, 2201796.
[19] Sykes, E. C. H.; Christopher, P.; Li, J. Fundamental insights into heterogeneous single-atom catalysis. *J. Chem. Phys.* **2021**, *155*, 210401.
[20] Chu, T. S.; Wang, G. Y.; Zhang, X. Y.; Jia, Y. Y.; Dai, S.; Liu, X. Z.; Zhang, L.; Yang, X.; Zhang, B. W.; Xuan, F. Z. High-density dual-structure single-atom Pt electrocatalyst for efficient hydrogen evolution and multimodal sensing. *Nano Lett.* **2024**, *24*, 9666–9674.
[21] Zhou, L.; Tian, P. F.; Zhang, B. W.; Xuan, F. Z. Data-driven rational design of single-atom materials for hydrogen evolution and sensing. *Nano Res.* **2023**, *17*, 3352–3358.
[22] Chen, Y. Q.; Zhang, J. R.; Yang, L. J.; Wang, X. Z.; Wu, Q.; Hu, Z. Recent advances in non-precious metal-nitrogen-carbon single-site catalysts for CO_2 electroreduction reaction to CO. *Electrochem. Energy Rev.* **2022**, *5*, 11.
[23] Ren, W. H.; Tan, X.; Jia, C.; Krammer, A.; Sun, Q.; Qu, J. T.; Smith, S. C.; Schueler, A.; Hu, X. L.; Zhao, C. Electronic regulation of nickel single atoms by confined nickel nanoparticles for energy-efficient CO_2 electroreduction. *Angew. Chem., Int. Ed.* **2022**, *61*, e202203335.
[24] Ren, W. H.; Tan, X.; Yang, W. F.; Jia, C.; Xu, S. M.; Wang, K. X.; Smith, S. C.; Zhao, C. Isolated diatomic Ni-Fe metal-nitrogen sites for synergistic electroreduction of CO_2. *Angew. Chem., Int. Ed.* **2019**, *58*, 6972–6976.
[25] Pan, F. P.; Deng, W.; Justiniano, C.; Li, Y. Identification of champion transition metals centers in metal and nitrogen-codoped carbon catalysts for CO_2 reduction. *Appl. Catal. B* **2018**, *226*, 463–472.
[26] Li, J. K.; Pršlja, P.; Shinagawa, T.; Martín Fernández, A. J.; Krumeich, F.; Artyushkova, K.; Atanassov, P.; Zitolo, A.; Zhou, Y. C.; García-Muelas, R. et al. Volcano trend in electrocatalytic CO_2 reduction activity over atomically dispersed metal sites on nitrogen-doped carbon. *ACS Catal.* **2019**, *9*, 10426–10439.
[27] Hu, X. M.; Hval, H. H.; Bjerglund, E. T.; Dalgaard, K. J.; Madsen, M. R.; Pohl, M. M.; Welter, E.; Lamagni, P.; Buhl, K. B.; Bremholm, M. et al. Selective CO_2 reduction to CO in water using earth-abundant metal and nitrogen-doped carbon electrocatalysts. *ACS Catal.* **2018**, *8*, 6255–6264.
[28] Pan, F. P.; Zhang, H. G.; Liu, K. X.; Cullen, D.; More, K.; Wang, M. Y.; Feng, Z. X.; Wang, G. F.; Wu, G.; Li, Y. Unveiling active sites of CO_2 reduction on nitrogen-coordinated and atomically dispersed iron and cobalt catalysts. *ACS Catal.* **2018**, *8*, 3116–3122.
[29] Wang, X. S.; Pan, Y. Y.; Ning, H.; Wang, H. M.; Guo, D. L.; Wang, W. H.; Yang, Z. X.; Zhao, Q. S.; Zhang, B. X.; Zheng, L. R. et al. Hierarchically micro- and meso-porous Fe-N_4O-doped carbon as robust electrocatalyst for CO_2 reduction. *Appl. Catal. B* **2020**, *266*, 118630.
[30] Li, Z.; Jiang, J. X.; Liu, X. M.; Zhu, Z. Z.; Wang, J. J.; He, Q.; Kong, Q. Q.; Niu, X. B.; Chen, J. S.; Wang, J. et al. Coupling atomically dispersed Fe-N_5 sites with defective N-doped carbon boosts CO_2 electroreduction. *Small* **2022**, *18*, 2203495.
[31] Li, K.; Zhang, S. B.; Zhang, X. L.; Liu, S.; Jiang, H. S.; Jiang, T. L.; Shen, C. Y.; Yu, Y.; Chen, W. Atomic tuning of single-atom Fe-N-C catalysts with phosphorus for robust electrochemical CO_2 reduction. *Nano Lett.* **2022**, *22*, 1557–1565.
[32] Wang, X. C.; Zhang, N.; Guo, S. H.; Shang, H. S.; Luo, X.; Sun, Z. Y.; Wei, Z. H.; Lei, Y. T.; Zhang, L. L.; Wang, D. et al. p-d Orbital hybridization induced by asymmetrical FeSn dual atom sites promotes the oxygen reduction reaction. *J. Am. Chem. Soc.* **2024**, *146*, 21357–21366.
[33] Wang, X. C.; Kang, Z. W.; Wang, D.; Zhao, Y. F.; Xiang, X.; Shang, H. S.; Zhang, B. Electronic structure regulation of the Fe-based single-atom catalysts for oxygen electrocatalysis. *Nano Energy* **2024**, *121*, 109268.
[34] Zhang, L. L.; Zhang, N.; Shang, H. S.; Sun, Z. Y.; Wei, Z. H.; Wang, J. T.; Lei, Y. T.; Wang, X. C.; Wang, D.; Zhao, Y. F. et al. High-density asymmetric iron dual-atom sites for efficient and stable electrochemical water oxidation. *Nat. Commun.* **2024**, *15*, 9440.
[35] Liu, C. H.; Wu, Y.; Sun, K. A.; Fang, J. J.; Huang, A. J.; Pan, Y.; Cheong, W. C.; Zhuang, Z. W.; Zhuang, Z. B.; Yuan, Q. H. et al. Constructing FeN_4/graphitic nitrogen atomic interface for high-efficiency electrochemical CO_2 reduction over a broad potential window. *Chem* **2021**, *7*, 1297–1307.
[36] Jia, C.; Zhao, Y.; Song, S.; Sun, Q.; Meyer, Q.; Liu, S. Y.; Shen, Y. S.; Zhao, C. Highly ordered hierarchical porous single-atom Fe catalyst with promoted mass transfer for efficient electroreduction of CO_2. *Adv. Energy Mater.* **2023**, *13*, 2302007.
[37] Yu, K.; Sun, K. A.; Cheong, W. C.; Tan, X.; He, C.; Zhang, J. Q.; Li, J. Z.; Chen, C. Oxalate-assisted synthesis of hollow carbon nanocage with Fe single atoms for electrochemical CO_2 reduction. *Small* **2023**, *19*, 2302611.
[38] Chen, G. B.; Lu, R. H.; Li, C. Z.; Yu, J. M.; Li, X. D.; Ni, L. M.; Zhang, Q.; Zhu, G. Q.; Liu, S. W.; Zhang, J. X. et al. Hierarchically porous carbons with highly curved surfaces for hosting single metal FeN_4 sites as outstanding oxygen reduction catalysts. *Adv. Mater.* **2023**, *35*, 2300907.
[39] Nam, D. H.; Bushuyev, O. S.; Li, J.; De Luna, P.; Seifitokaldani, A.; Dinh, C. T.; García de Arquer, F. P.; Wang, Y. H.; Liang, Z. Q.; Proppe, A. H. et al. Metal-organic frameworks mediate Cu coordination for selective CO_2 electroreduction. *J. Am. Chem. Soc.* **2018**, *140*, 11378–11386.
[40] Cui, T. T.; Wang, Y. P.; Ye, T.; Wu, J.; Chen, Z. Q.; Li, J.; Lei, Y. P.; Wang, D. S.; Li, Y. D. Engineering dual single-atom sites on 2D ultrathin N-doped carbon nanosheets attaining ultra-low-temperature zinc-air battery. *Angew. Chem., Int. Ed.* **2022**, *61*, e202115219.
[41] Tang, J.; Salunkhe, R. R.; Liu, J.; Torad, N. L.; Imura, M.; Furukawa, S.; Yamauchi, Y. Thermal conversion of core-shell metal-organic frameworks: A new method for selectively functionalized nanoporous hybrid carbon. *J. Am. Chem. Soc.* **2015**, *137*, 1572–1580.
[42] Fechler, N.; Fellinger, T. P.; Antonietti, M. "Salt templating": A simple and sustainable pathway toward highly porous functional carbons from ionic liquids. *Adv. Mater.* **2013**, *25*, 75–79.
[43] Liu, X. F.; Fechler, N.; Antonietti, M. Salt melt synthesis of ceramics, semiconductors and carbon nanostructures. *Chem. Soc. Rev.* **2013**, *42*, 8237–8265.
[44] Mohd Adli, N.; Shan, W. T.; Hwang, S.; Samarakoon, W.; Karakalos, S.; Li, Y.; Cullen, D. A.; Su, D.; Feng, Z. X.; Wang, G. F. et al. Engineering atomically dispersed FeN_4 active sites for CO_2 electroreduction. *Angew. Chem., Int. Ed.* **2021**, *60*, 1022–1032.
[45] Zhang, J. T.; Zhao, Z. H.; Xia, Z. H.; Dai, L. M. A metal-free bifunctional electrocatalyst for oxygen reduction and oxygen evolution reactions. *Nat. Nanotechnol.* **2015**, *10*, 444–452.
[46] Wang, H. J.; Wu, X. D.; Liu, G. Y.; Wu, S. Y.; Xu, R. Bimetallic MOF derived nickel nanoclusters supported by nitrogen-doped carbon for efficient electrocatalytic CO_2 reduction. *Nano Res.* **2023**, *16*, 4546–4553.
[47] Zhou, Y.; Xie, M. X.; Song, Y.; Yan, D. K.; Wang, Z. L.; Zhang, S.; Deng, C. Edge-enriched Ni-N_4 atomic sites embedded enoki-mushroom-like carbon nanotubes assembling hollow fibers for CO_2

conversion and flexible Zn-air battery. *Energy Storage Mater.* **2022**, *47*, 235–248.

[48] Wang, W.; Chen, K. Y.; Sun, Y.; Zhou, S. Q.; Zhang, M.; Yuan, J. Y. Mesoporous Ni-N-C as an efficient electrocatalyst for reduction of CO_2 into CO in a flow cell. *Appl. Mater. Today* **2022**, *29*, 101619.

[49] Zhao, Y. Z.; Miao, Z. C.; Wang, F. Y.; Liang, M. F.; Liu, Y.; Wu, M.; Diao, L. C.; Mu, J. L.; Cheng, Y. Z.; Zhou, J. N-doped carbon-encapsulated nickel on reduced graphene oxide materials for efficient CO_2 electroreduction to syngas with potential-independent H_2/CO ratios. *J. Environ. Chem. Eng.* **2021**, *9*, 105515.

[50] Thommes, M.; Kaneko, K.; Neimark, A. V.; Olivier, J. P.; Rodriguez-Reinoso, F.; Rouquerol, J.; Sing, K. S. W. Physisorption of gases, with special reference to the evaluation of surface area and pore size distribution (IUPAC Technical Report). *Pure Appl. Chem.* **2015**, *87*, 1051–1069.

[51] Chen, Y.; Zhao, J.; Pan, X. L.; Li, L.; Yu, Z. N.; Wang, X. D.; Ma, T. Y.; Lin, S.; Lin, J. Tuning the inter-metal interaction between Ni and Fe atoms in dual-atom catalysts to boost CO_2 electroreduction. *Angew. Chem., Int. Ed.* **2024**, *63*, e202411543.

[52] Cao, C. S.; Zhou, S. H.; Zuo, S. W.; Zhang, H. B.; Chen, B.; Huang, J. H.; Wu, X. T.; Xu, Q.; Zhu, Q. L. Si doping-induced electronic structure regulation of single-atom Fe sites for boosted CO_2 electroreduction at low overpotentials. *Research* **2023**, *6*, 0079.

[53] Chen, G. B.; An, Y.; Liu, S. W.; Sun, F. F.; Qi, H. Y.; Wu, H. F.; He, Y. H.; Liu, P.; Shi, R.; Zhang, J. et al. Highly accessible and dense surface single metal FeN_4 active sites for promoting the oxygen reduction reaction. *Energy Environ. Sci.* **2022**, *15*, 2619–2628.

[54] Zheng, W. Z.; Chen, F.; Zeng, Q.; Li, Z. J.; Yang, B.; Lei, L. C.; Zhang, Q. H.; He, F.; Wu, X. L.; Hou, Y. A universal principle to accurately synthesize atomically dispersed metal-N_4 sites for CO_2 electroreduction. *Nanomicro Lett.* **2020**, *12*, 108.

[55] Li, Y. Z.; Wei, B.; Zhu, M. H.; Chen, J. C.; Jiang, Q. K.; Yang, B.; Hou, Y.; Lei, L. C.; Li, Z. J.; Zhang, R. F. et al. Synergistic effect of atomically dispersed Ni-Zn pair sites for enhanced CO_2 electroreduction. *Adv. Mater.* **2021**, *33*, 2102212.

[56] Li, S. M.; Ceccato, M.; Lu, X. Y.; Frank, S.; Lock, N.; Roldan, A.; Hu, X. M.; Skrydstrup, T.; Daasbjerg, K. Incorporation of nickel single atoms into carbon paper as self-standing electrocatalyst for CO_2 reduction. *J. Mater. Chem. A* **2021**, *9*, 1583–1592.

[57] Chen, H. H.; Guo, X.; Kong, X. D.; Xing, Y. L.; Liu, Y.; Yu, B. L.; Li, Q. X.; Geng, Z. G.; Si, R.; Zeng, J. Tuning the coordination number of Fe single atoms for the efficient reduction of CO_2. *Green Chem.* **2020**, *22*, 7529–7536.

[58] Yang, Y.; Chen, L. Z.; Guo, Z. Y.; Liu, S. Q.; Wu, P. D.; Fang, Z.; Zhang, K.; Li, H. Remote p-d orbital hybridization via first/second-layer coordination of Fe single atoms with heteroatoms for enhanced electrochemical CO_2-to-CO reduction. *J. Mater. Chem. A* **2024**, *12*, 8991–9001.

[59] Liu, W. P.; Wang, K.; Gong, L.; Zhi, Q. J.; Jiang, R.; Liu, W. B.; Sun, T. T.; Zhang, Y. X.; Jiang, J. Z. Edge-located Fe-N_4 sites on porous Graphene-like nanosheets for boosting CO_2 electroreduction. *Chem. Eng. J.* **2022**, *431*, 134269.

[60] Wang, Y. T.; Li, Y. H.; Liu, J. Z.; Dong, C. X.; Xiao, C. Q.; Cheng, L.; Jiang, H. L.; Jiang, H.; Li, C. Z. $BiPO_4$-derived 2D nanosheets for efficient electrocatalytic reduction of CO_2 to liquid fuel. *Angew. Chem., Int. Ed.* **2021**, *60*, 7681–7685.

[61] Jiang, S. S.; Chen, Y.; Cui, X.; Sun, Y.; Ma, G. H.; Bao, Y. X.; Yao, Y. L.; Ma, T. Y. Constructing highly efficient ZnO nanocatalysts with exposed extraordinary (110) facet for CO_2 electroreduction. *ACS Appl. Mater. Interfaces* **2024**, *16*, 14965–14973.

[62] Ju, W.; Bagger, A.; Wang, X. L.; Tsai, Y. L.; Luo, F.; Möller, T.; Wang, H.; Rossmeisl, J.; Varela, A. S.; Strasser, P. Unraveling mechanistic reaction pathways of the electrochemical CO_2 reduction on Fe-N-C single-site catalysts. *ACS Energy Lett.* **2019**, *4*, 1663–1671.

[63] Leonard, N.; Ju, W.; Sinev, I.; Steinberg, J.; Luo, F.; Varela, A. S.; Roldan Cuenya, B.; Strasser, P. The chemical identity, state and structure of catalytically active centers during the electrochemical CO_2 reduction on porous Fe-nitrogen-carbon (Fe-N-C) materials. *Chem. Sci.* **2018**, *9*, 5064–5073.